Supplementary information for: Desert Power for the AI Era

Ziheng Zhu, Runxin Yu*, and Da Zhang*

*Corresponding author;
E-mail: runxinyu@outlook.com; zhangda@tsinghua.edu.cn.

August 6, 2025

Contents

List of Tables

List of Figures

1 Supplementary text

This section assesses the potential of renewable energy resources, specifically across onshore wind systems and utility-scale solar PV technologies. The resource assessment framework integrates two principal components: 1) hourly generation potential, defined by the capacity factor (CF∈[0,1])—the ratio of actual power output to nameplate capacity, which serves as a standardized metric for temporal variability and generation efficiency; and 2) maximum installation capacity (MW) per grid cell, derived by multiplying installation density (MW/km^2) with the technically suitable development area (km^2). High-resolution models, incorporating key meteorological parameters (wind speed, ambient temperature, air density, and surface-level shortwave solar radiation), facilitate the calculation of capacity factors. For wind and utility-scale solar PV, the analysis prioritizes the identification of viable land areas. This methodology yields a temporally resolved and spatially explicit characterization of renewable energy potentials, accurately reflecting atmospheric dynamics and land-use constraints.

1.1 Assessment of the hourly capacity factor for wind power

The determination of the hourly capacity factor for wind power generation hinges primarily on the interaction between the specific power output curve of the wind turbine and the wind speed as measured at hub height. This power output curve, in conjunction with a suite of additional technical specifications, forms the quantitative foundation for assessing the hourly capacity factor in wind power systems. Comprehensive technical parameters for diverse wind turbine configurations, including critical metrics like nameplate capacity, cut-in and cut-out wind speeds, rated wind speed, turbine hub elevation, and complete power output curves, are systematically compiled by the National Renewable Energy Laboratory (NREL) within its wind energy assessment initiative [1]. In the present study, the hourly capacity factor assessments for onshore wind employ the 2020 ATB NREL Reference 5.5 MW 175 turbine models. The pertinent parameters for these selected models are provided in Table S1.

The power output curve of a wind turbine is a piecewise function contingent upon the wind speed (v_w^h, m/s) at the turbine's hub height:

$$P(v_w^h) = \begin{cases} 0, & v_w^h < v_{\text{cut-in}} \text{ or } v_w^h \geq v_{\text{cut-out}} \\ f(v_w^h), & v_{\text{cut-in}} \leq v_w^h < v_{\text{rated}} \\ P_{\text{rated}}, & v_{\text{rated}} \leq v_w^h < v_{\text{cut-out}} \end{cases} \tag{S1-1}$$

where power generation remains zero when v_w^h falls below the cut-in threshold or exceeds the cut-out limit. Within the operational range between cut-in and rated wind speeds, the turbine's power generation demonstrates a monotonically increasing relationship with wind speed. Upon attaining or surpassing the rated wind speed and below the cut-out threshold, the turbine operates at maximum efficiency, producing power equivalent to its nameplate capacity. To facilitate our capacity factor analysis, we normalized the power output curves across various turbine configurations. Figure S2 illustrates these normalized output functions for multiple turbine variants documented by NREL [1]. Because the non-linear relationship between wind speed and power output only lies within the segment spanning from cut-in to rated wind speed, we implement a third-degree polynomial regression methodology to fit a power output to wind speed function in this interval, with the fitted results shown in Figure S3.

Wind speed at the turbine hub height is a fundamental variable for assessing the hourly capacity factor of wind power. We adopt the re-analysis meteorological data from the European Centre for Medium-Range Weather Forecasts Reanalysis Version 5 (ERA5) dataset, which provides a comprehensive global climate record spanning over eight decades (1940–current), with a spatial resolution of 0.25° × 0.25° and hourly temporal resolution [2]. The wind speed data from ERA5 contains 10 m and 100 m heights (U10m, V10m, U100m, and V100m, m/s). In this study, the hub heights of turbine models selected for output assessment are 120 m for onshore wind power (see Table S1), which are not available directly in the ERA5 dataset. Therefore, we employ the vertical power law profile to estimate the target wind speed:

$$v_w^h = v_w^{100} \times (\frac{z_h}{z_{100}})^{\alpha}, \tag{S1-2}$$

where v_w^h is the wind speed at height h (m/s), v_w^{100} is the wind speed at 100 m (m/s) calculated as $v_w^{100} = \sqrt{U_{100}^2 + V_{100}^2}$, z_h is the target height (120 m for onshore wind), $z_{100} = 100$ m, and α is the wind shear coefficient, which varies with terrain. We apply Equation S1-2 using wind speeds at 10 m and 100 m to estimate α for each hour at each 0.25° × 0.25° grid cell [3].

A wind turbine's power output curve is standardized based on measurements performed at a standard air density (ρ_{std}^h=1.225 kg/m^3). Hence, calculating power output at a given time step using this curve requires converting the observed wind speed to the equivalent wind speed at standard air density. The relationship between the wind speed under standard conditions (v_{std}^h) and the measured wind speed (v_{meas}^h) is defined by the following equation [4]:

$$v_{std}^h = v_{meas}^h \times \left(\frac{\rho_{meas}^h}{\rho_{std}^h} \right)^{1/3}, \tag{S1-3}$$

this equation defines v_{std}^h as the wind speed at height h under standard air density, where v_{meas}^h represents the measured wind speed derived from Equation S1-2, and ρ_{meas}^h denotes the actual air density. However, ERA5 reanalysis data do not directly provide observed air density. Instead, air density is calculated using the ideal gas state equation, based on other reported meteorological variables [4]:

$$\rho_{meas}^h = \frac{p_{meas}^h - p_{vapour}}{R_{dry} T} + \frac{p_{vapour}}{R_{vapour} T}, \tag{S1-4}$$

where R_{dry} denotes the gas constant for dry air, which is 287.1 J/kg $\cdot$ K, and R_{vapour} represents the specific gas constant for water vapor, equivalent to 461.5 J/kg $\cdot$ K. Furthermore, p_{meas}^h signifies the measured atmospheric pressure in Pascals (Pa) at hub height (h), p_{vapour} indicates the partial pressure of water vapor (Pa) at a height of 2 meters, and T refers to the temperature in Kelvin (K) at hub height. The determination of the partial pressure of water vapor, p_{vapour}, relies on the air's relative humidity (ϕ, expressed in %) and temperature, using the Clausius-Clapeyron equation:

$$p_{vapour} = \phi \times 610.78 \times \exp\left(\frac{17.27(t - 273.15)}{t - 273.15 + 237.3} \right), \tag{S1-5}$$

where t represents the temperature at a 2 m height. It is assumed that the partial pressure of water vapor at hub height is equivalent to that at 2 m [4]. And the air humidity, ϕ, is calculated from the dewpoint temperature (K) at a 2 m height, as provided by ERA5 data, using the equation presented by [5]:

$$\phi = \exp\left(\frac{17.625 \times (t_d - 273.15)}{243.04 + (t_d - 273.15)} - \frac{17.625 \times (t - 273.15)}{243.04 + (t - 273.15)} \right) \times 100\%. \tag{S1-6}$$

Finally, we calculate the atmospheric pressure (Pa) at hub height (h), denoted as p_{meas}^h, using the surface pressure from ERA5 (Pa, p_0), by:

$$p_{meas}^h = p_0 \times e^{-\frac{gh}{R_d t}}, \tag{S1-7}$$

where e is the base of the natural logarithm, g = 9.81 m/s^2 is the gravitational acceleration at the Earth's surface, t is the temperature at 2 m height, and R_d is a function of the specific humidity of the air (q, kg/m^3):

$$R_d = qR_{vapour} + \frac{R_{dry}}{1 + q}. \tag{S1-8}$$

Following the acquisition of wind speed at hub height under standard air density via the aforementioned calculations, the hourly capacity factor for wind power generation is determined for each 0.25° × 0.25° cell using the normalized power output curve of the specified wind turbine model. Subsequent adjustments to this capacity factor are implemented based on the ensuing considerations:

- The capacity factor at each timestep undergoes a 5% reduction to account for phenomena such as wake effects and electrical losses within wind farms [6, 7].

- Wind turbine operation ceases when the temperature at hub height falls below −30°C due to extreme cold conditions, necessitating a correction of the capacity factor to 0 [4].
- The wind turbine halts operation if the wind speed exceeds the cut-out threshold. Reactivation occurs only when specific wind speed criteria are met. We address this by employing a hysteresis window approach, wherein turbine operation resumes only after the wind speed first decreases to or below 20 m/s following a shutdown. The cut-out threshold for the wind turbine is detailed in Table S1.

1.2 Assessment of the hourly capacity factor for solar photovoltaic power

We adopt the fixed-tilt photovoltaic system model [8] to quantify the hourly capacity factor of solar PV power at a given grid cell [9]. The solar PV power output constitutes a fraction of the nameplate capacity, which can be derived from meteorological data. Specifically, we use surface downwelling shortwave radiation (SSRD2M, J/m^2), surface temperature (T2m, K), and 10-meter height surface wind speed (U10m and V10m, m/s) at a 0.25°×0.25° spatial resolution from ERA5 [2]. Based on these inputs, we assess the DC power output to the nameplate capacity fraction using the following equation [10]:

$$\frac{P_{dc}}{P_{dc0}} = [1 + \gamma \times (T_{cell}(t) - T_{std})] \times \frac{ssrd(t)}{ssrd_{std}} \times \eta_{sys}, \tag{S1-9}$$

where P_{dc}/P_{dc0} represents the ratio of the DC power output to the nameplate capacity. $T_{cell}(t)$ denotes the cell temperature of the solar PV module, and T_{std} is its counterpart under standard test conditions (25 °C). The temperature coefficient of the solar PV cell, γ, is set to -0.005 °C^{-1}, reflecting the module's efficiency variations with temperature. $ssrd(t)$ indicates the hourly surface downwelling shortwave radiation (W/m^2, converted from J/m^2) in the ambient environment, which is derivable from the SSRD2M variable in the ERA5 dataset. The term $ssrd_{std}$ signifies the shortwave radiation flux incident on the solar PV panel under standard test conditions, defined as 1,000 W/m^2. Lastly, $\eta_{sys} \in [0, 1]$ represents the efficiency of the DC electrical system, set to 0.86 [10, 11].

Consistent with previous studies [3, 12], the solar PV cell temperature ($T_{cell}(t)$, °C) is calculated based on surface downwelling shortwave radiation ($ssrd(t)$, W/m^2), ambient temperature ($T(t)$, °C), and wind speed ($v_w(t)$, m/s) using Equation S1-10:

$$T_{cell}(t) = c_1 + c_2 \times T(t) + c_3 \times ssrd(t) + c_4 \times v_w(t). \tag{S1-10}$$

In this equation, $T(t)$ denotes the hourly ambient temperature and $v_w(t)$ represents the hourly surface wind speed. The coefficients are $c_1 = 4.3$ °C, $c_2 = 0.943$, $c_3 = 0.028$ °C·m^2·W^{-1}, and $c_4 = -1.528$ °C·s·m^{-1}. The substitution of $T_{cell}(t)$ from Equation S1-10 into Equation S1-9 (which defines P_{dc}/P_{dc0} as a function of $T_{cell}(t)$, $ssrd(t)$, and system parameters) and subsequent algebraic rearrangement yields Equation S1-11:

$$\frac{P_{dc}}{P_{dc0}} = [\alpha_1 \times ssrd(t) + \alpha_2 \times ssrd(t)^2 + \alpha_3 \times ssrd(t) \times T(t) + \alpha_4 \times ssrd(t) \times v_w(t)] \times \eta_{sys}. \tag{S1-11}$$

Here, the coefficients $\alpha_1, \alpha_2, \alpha_3$, and α_4 are 1.1035×10^{-3}, -1.4×10^{-7}, -4.715×10^{-6}, and 7.64×10^{-6}, respectively. The resulting ratio P_{dc}/P_{dc0} is a dimensionless quantity. The fraction of AC output to the nameplate AC capacity, P_{ac}/P_{ac0}, is derived according to the PVWatts model [11] using Equation S1-12:

$$\frac{P_{ac}}{P_{ac0}} = \min\left(\eta \times \frac{P_{dc}}{P_{ac0}}, 1\right). \tag{S1-12}$$

In this context, P_{ac0} is the nameplate AC capacity, defined as $P_{ac0} = \eta_{nom} \times P_{dc0}$, where $\eta_{nom} = 0.96$ is the nominal DC-AC inverter efficiency. The term η represents the inverter efficiency, which is a function of P_{dc}/P_{dc0} (the ratio of DC output to nameplate DC capacity). The inverter performance characteristic is described by Equation S1-13 [11]:

$$\eta = \frac{\eta_{nom}}{\eta_{ref}} \times \left(-0.0162 \times \zeta - \frac{0.0059}{\zeta} + 0.9858 \right). \tag{S1-13}$$

Here, $\zeta = P_{dc}/P_{dc0}$ represents the ratio of DC output to nameplate DC capacity, and $\eta_{ref} = 0.9637$ is the reference inverter efficiency. By combining Equations S1-11, S1-12, and S1-13, the fraction of the AC output to the nameplate AC capacity, P_{ac}/P_{ac0}, is expressed as:

$$\frac{P_{ac}}{P_{ac0}} = \min \left(\frac{1}{\eta_{ref}} \times (-0.0162 \times \zeta^2 + 0.9858 \times \zeta - 0.0059), 1 \right). \tag{S1-14}$$

1.3 Assessment of suitable area for developing wind, utility-scale solar photovoltaic power

We estimate the installation capacity potential of wind and solar power based on the suitable land area (km^2) and assumed installation density (MW/km^2) [13, 14] for each 0.25° × 0.25° grid cell, consistent with the resolution of the ERA5 meteorological data. To evaluate the suitable land area, we use the global 300 m gridded land cover data in 2020, provided by the European Space Agency (ESA) [15], which is represented at the "pixel" level within each grid cell. The ESA land cover dataset provides global maps describing the land surface into 22 classes, which have been defined using the United Nations Food and Agriculture Organization's (UN FAO) Land Cover Classification System (LCCS). See the definition of each land use type in Table S2. In addition to the land cover maps, several quality flags, including nature reserve and biodiversity reserve area, slope, altitude, shipping lanes, and water depth, are adopted to document the suitable land area recognition. Using this land cover dataset as the base map, we first exclude the pixels within each grid cell that are situated in nature reserves and biodiversity reserve areas due to environmental protection reasons. Subsequently, we formulate three scenarios (open, base, and conservative) to further eliminate the remaining pixels that do not meet natural condition constraints such as steep slopes, high altitudes, and water depths. Following these steps, the suitability factor is devised to estimate the suitable area within the remaining pixels based on land use types to represent different policy requirements. Finally, we aggregate the suitable area of qualified pixels in each grid cell to determine the total suitable area for developing wind and utility-scale solar PV power.

Upon excluding pixels within protected areas, or those constrained by natural conditions or shipping safety, the suitable area of the retained pixels is determined by applying a land-use-specific suitability factor [9, 13, 14, 16, 17]. This factor represents the fraction of a pixel's area suitable for deployment and is provided for each land use type in Table S2. The total suitable area for wind and utility-scale solar PV within each grid cell is subsequently calculated by aggregating the suitable areas of all included pixels. The spatial distribution of the resulting suitable areas for wind and utility-scale solar PV is depicted in Figure S4 and Figure S5, respectively.

1.4 Assessment of installation capacity potential

The installation capacity potential (MW) for wind and solar PV power is determined by the product of the available deployment area (in km^2) and the technology-specific power installation density (in MW/km^2). Mathematically, this relationship is stated as:

$$Cap_g^{max} = SA \times \mathcal{D}_g, \tag{S1-15}$$

where Cap_g^{max} is the installation capacity potential (MW) for generator g, SA denotes the geospatially resolved suitable installation area (km^2) within each grid cell, and $\mathcal{D}_g$ signifies the technology-specific installation density (MW/km^2) characteristic of generator g.

1.4.1 Wind power

Wind turbine spacing represents a significant factor in wind farm layout, affecting both power generation and turbine structural integrity. The optimal spacing largely depends on the dominant wind direction and turbine rotor diameter. Previous research indicates that spacing of 5–10 rotor diameters between turbines helps to alleviate wake effects and turbine fatigue [6, 18]. In this study, we consider utility-scale turbines with nameplate capacities above 1 MW. Installation densities are computed utilizing NREL turbine specifications [1] and a 7×7 rotor diameter spacing configuration [6, 19]. This yields onshore wind power installation densities ranging from 2.40 to 5.50 MW/km^2. Table S3 provides the details of these ranges. For the assessment of wind power potentials, we adopt reference installation densities of 4.0 MW/km^2 for onshore wind [6], consistent with the definition in Equation S1-15. Figure S7 shows the resulting installation capacity potential (MW) for onshore wind for each grid cell in the desert area. The annual power generation potential is then determined by the installation capacity potential multiplied by the annual average capacity factor.

1.4.2 Solar power

In this study, we assume a fixed tilt model for the installation of solar PV panels to assess the capacity potential of solar PV power, see the installation schematic diagram in Figure S6. Under this assumption, it is imperative to calculate the optimal tilt, orientation, and inter-panel distance in each grid cell. Initially, we determine the corresponding optimal tilt based on the latitude of each grid cell as below [13]:

$$\Sigma = \begin{cases} 1.3793 + \theta(1.2011 + \theta(-0.014404 + \theta \times 0.000080509)), & (R = 0.96,\ \text{North Hemisphere}) \\ -0.41657 + \theta(1.4216 + \theta(0.024051 + \theta \times 0.00021828)), & (R = 0.97,\ \text{South Hemisphere}) \end{cases} \tag{S1-16}$$

where θ is the latitude of the grid cell. In assessing the solar PV resource potential, it is hypothesized that the PV arrays are oriented facing the equator to maximize solar radiation receipt. Inter-panel spacing can be determined by avoiding shading from adjacent panels. Given that shadows reach maximum length in the Northern Hemisphere on the winter solstice at 3 PM, the solar altitude and azimuth at this time are adopted to evaluate the inter-panel distance of utility-scale solar PV to preclude potential shading concerns. Similarly, the 3 PM at the southern winter solstice is used for grid cells in the southern hemisphere. The equation for computing the separation between adjoining PV panels is [8]:

$$D = L \times \left(\cos\Sigma + \frac{\sin\Sigma}{\tan\beta_n} \times \cos\phi_s\right), \tag{S1-17}$$

where D is the distance between adjacent PV panels, L is the length of the PV panel, Σ is the optimal tilt angle in radians, β_n and ϕ_s are the solar altitude angle and azimuth angle, respectively. After determining the distance D, we can calculate the packing factor, which represents the ratio of the area occupied by PV panels to the installation area, as follows:

$$PF = \frac{L}{D} = \frac{1}{\cos\Sigma + \frac{\sin\Sigma}{\tan\beta_n} \times \cos\phi_s}. \tag{S1-18}$$

Finally, we assume a unit capacity of 161.9 W/m^2 [13] and determine the installation density for solar power in each grid cell by multiplying it with the packing factor, denoted as $\mathcal{D}_{pv} = 161.9 \times PF$. We show the resulting installation capacity potential (MW) for solar PV in each cell in Figure S9.

2 Supplementary tables

Table S1: Technical parameters of the wind turbine selected by this assessment.

	2020ATB NREL Reference 5.5MW 175	IEA 15MW 240 RWT
Nameplate capacity (MW)	5.5	15.0
Hub height (m)	120.0	150.0
Cut-in wind speed (m/s)	3.25	3.00
Cut-out wind speed (m/s)	25.0	25.0
Rated wind speed (m/s)	10.0	10.6

Table S2: Suitability factor (%) of each land use type for determining suitable areas for onshore wind and utility-scale solar PV.

ID	Label	Solar PV	Wind
10	Cropland, rainfed	5	80
20	Cropland, irrigated or post-flooding	0	0
30	Mosaic cropland (>50%) natural vegetation (tree, shrub, herbaceous cover) (<50%)	0	10
40	Mosaic natural vegetation (tree, shrub, herbaceous cover) (>50%)/cropland (<50%)	5	10
50	Tree cover, broadleaved, evergreen, closed to open (>15%)	5	10
60	Tree cover, broadleaved, deciduous, closed to open (>15%)	5	10
70	Tree cover, needleleaved, evergreen, closed to open (>15%)	5	10
80	Tree cover, needleleaved, deciduous, closed to open (>15%)	5	10
90	Tree cover, mixed leaf type (broadleaved and needleleaved)	5	10
100	Mosaic tree and shrub (>50%) / herbaceous cover (<50%)	20	90
110	Mosaic herbaceous cover (>50%) / tree and shrub (<50%)	20	90
120	Shrubland	5	60
130	Grassland	5	80
140	Lichens and mosses	0	0
150	Sparse vegetation (tree, shrub, herbaceous cover) (<15%)	20	90
160	Tree cover, flooded, fresh or brackish water	0	10
170	Tree cover, flooded, saline water	0	10
180	Shrub or herbaceous cover, flooded, fresh/saline/brackish water	0	10
190	Urban areas	0	0
200	Bare areas	40	90
210	Water bodies	0	0
220	Permanent snow and ice	0	0

Table S3: Onshore wind turbine parameters.

Wind turbine model	Rotor diameter (m)	Nameplate capacity (MW)	Installation density (MW/km^2)
2020 ATB NREL Reference 5.5 MW	175.0	5.50	3.60
2020 ATB NREL Reference 7 MW	200.0	7.00	3.50
BAR BAU LowSP 3.25 MW	166.0	3.25	2.40
BAR BAUa 5 MW	167.4	5.00	3.60
BAR LBNL-IEA 3.3 MW	156.0	3.30	2.72
BAR HighSP 5 MW	135.0	5.00	5.50
BAR LowSP 4.5 MW	194.0	4.50	2.40
BAR LowSP 6.5 MW	234.0	6.50	2.40
DOE GE 1.5 MW	77.0	1.50	5.00
IEA 3.4 MW Reference	130.0	3.37	4.00

Table S4: Regional-level wind and solar resource potential in desert areas.

Region	Solar PV		Wind	
	Capacity (GW)	Generation (TWh/yr)	Capacity (GW)	Generation (TWh/yr)
Afghanistan	5783.3	12179.1	1263.8	1848.8
Algeria	69334.4	152637.3	6650.7	19052.4
Angola	620.9	1392.3	113.7	55.5
Australia	42802.4	90581.1	8414.5	26084.6
Azerbaijan	180.4	286.6	81.6	64.9
Barbados	0.7	1.5	0.3	1.4
Botswana	1303.8	2803.8	559.9	1124.3
Chad	16066.2	38112.1	1427.9	4308.8
Chile	2558.5	6325.5	335.2	80.1
China	28658.3	55830.0	5334.6	8352.9
Colombia	202.7	432.7	46.0	165.0
Cuba	4.4	8.9	2.0	2.4
Djibouti	656.9	1340.9	65.4	86.9
Egypt	27469.8	62337.2	2583.2	6077.3
Eritrea	1135.3	2338.1	120.6	130.1
Ethiopia	2776.8	5647.8	326.8	279.8
Georgia	14.0	22.3	8.7	3.5
Guatemala	3.4	6.0	3.2	0.1
Hala'ib Triangle	3.4	7.6	0.4	0.7
India	2624.0	4828.3	1257.2	1675.7
Iran	20543.1	42457.8	2710.1	3151.7
Iraq	10029.8	20442.5	1118.9	2756.6
Israel	227.6	466.8	30.4	33.1
Jammu-Kashmir	2.4	4.2	2.1	0.2
Jordan	1935.8	4128.5	204.3	410.1
Kazakhstan	10881.4	17666.3	4267.8	14010.0
Kuwait	500.8	1039.6	47.8	146.8
Kyrgyzstan	2.0	3.4	1.1	0.6
Libyan Arab Jamahiriya	59758.6	133962.3	5537.7	14153.8
Madagascar	1514.2	3171.5	273.5	430.7
Mali	19488.1	43866.0	1539.1	4648.8

Table S4 continued from previous page

Region	Solar PV		Wind	
Martinique	0.1	0.3	0.1	0.1
Ma’tan al-Sarra	56.7	129.3	5.1	13.6
Mauritania	24299.7	54959.6	1968.8	6678.6
Mexico	2644.0	5682.7	1392.2	1652.8
Mongolia	9153.3	16926.4	1911.7	3654.8
Morocco	1102.4	2413.3	127.4	239.3
Namibia	2622.3	6009.8	1025.5	1787.7
Netherlands Antilles	1.0	2.3	0.3	1.9
Niger	17792.9	41517.0	1423.1	3966.4
Oman	10531.9	22794.0	860.5	1714.4
Pakistan	6531.0	13762.6	1228.2	1452.7
Peru	2038.1	4588.0	390.8	110.8
Qatar	288.9	610.0	24.8	59.0
Russian Federation	227.2	344.1	249.2	738.0
Saudi Arabia	57936.7	127044.7	5284.4	10723.6
Somalia	1167.1	2437.9	206.9	533.0
South Africa	3421.1	7512.6	1303.4	2922.0
Sri Lanka	4.1	8.0	1.2	4.2
Sudan	22901.1	53858.6	1877.6	5426.4
Syrian Arab Republic	1669.8	3401.0	186.8	395.3
Tajikistan	18.9	34.3	6.1	2.0
Tunisia	1799.7	3722.7	202.7	572.8
Turkmenistan	7818.6	14270.0	1200.2	3238.3
United Arab Emirates	1975.2	4202.8	171.7	322.0
United States of America	4170.4	8706.9	2570.8	3416.6
Uzbekistan	4963.7	8799.8	852.8	2458.0
Venezuela	346.8	698.0	127.5	146.1
West Bank	4.1	8.1	1.4	0.8
Western Sahara	11405.1	25887.4	971.6	4425.8
Yemen	12869.8	28553.1	1326.2	1884.0
Zimbabwe	1.0	1.9	0.4	0.4
Total	536845.7	1163215.2	71228.1	167679.5

Table S5: Performance parameters used for storage system in this study.

Feature	Duration (h)	Charge efficiency (%)	Discharge efficiency (%)	Self-discharge rate (%)
Parameter	4	95	95	0

Table S6: Investment costs for wind, solar, and storage used in this study as the current level.

Region	Onshore Wind ($/kW)	Solar PV ($/kW)	Storage ($/kW)
Africa	1200	758	1144
Asia (excluding China and India)	1115	583	1000
China	600	493	286
Europe	1560	1080	1200
India	840	486	520
North America	1700	1000	1144
Oceania	1522	736	1590
South America	835	743	1358

Table S7: Investment cost projection (ratio to the current level) to 2030 for wind, solar, and storage.

Scenario	Onshore wind	Solar PV	Storage
CapEx-High	0.83	0.81	0.83
CapEx-Mid	0.71	0.64	0.625
CapEx-Low	0.60	0.44	0.42

Table S8: Electricity cost ($/kWh) in conventional mode for data center.

Region	Africa	Asia (excluding China and India)	China	Europe	India	North America	Oceania	South America
Cost	0.2	0.142	0.1	0.2	0.13	0.24	0.171	0.165

3 Supplementary figures

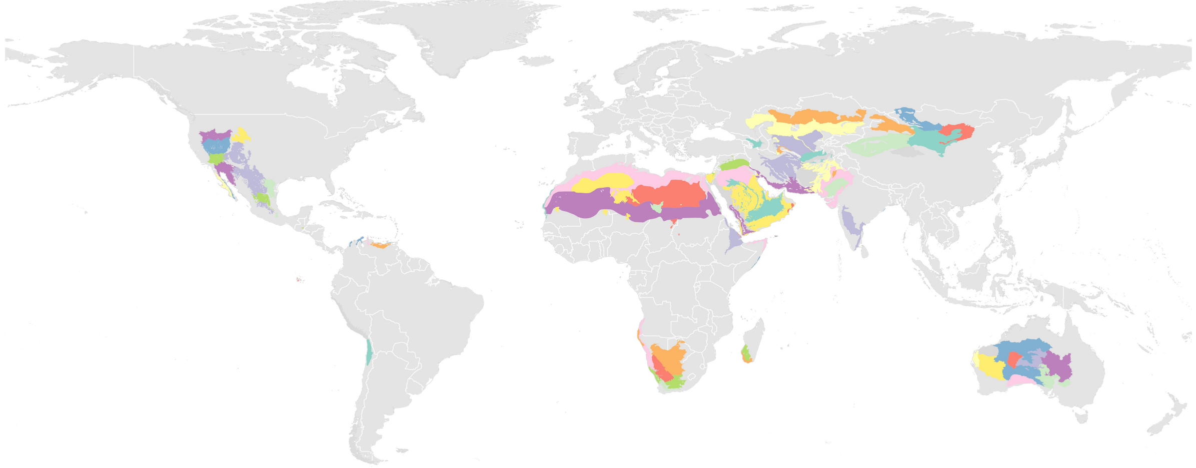

Figure S1: Desert area used in this study.

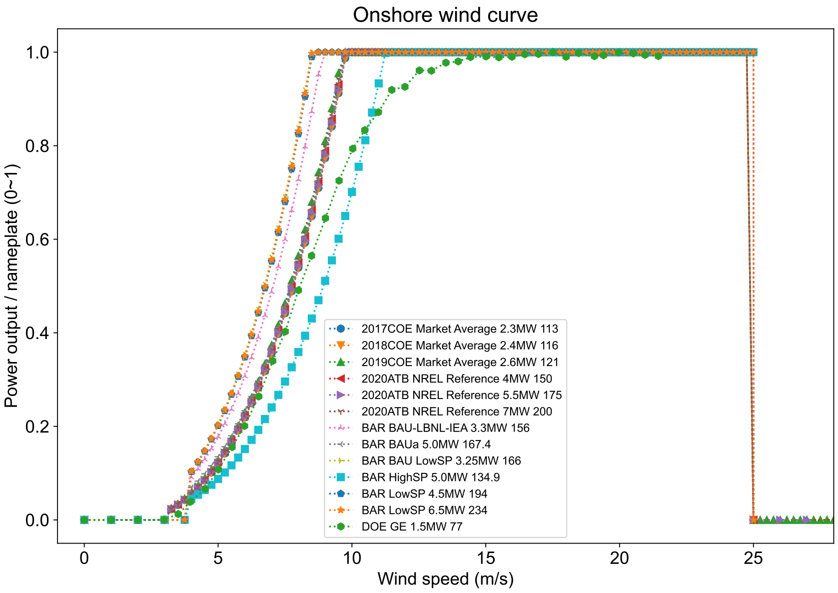

Figure S2: Normalized power output curve of different wind power models [1].

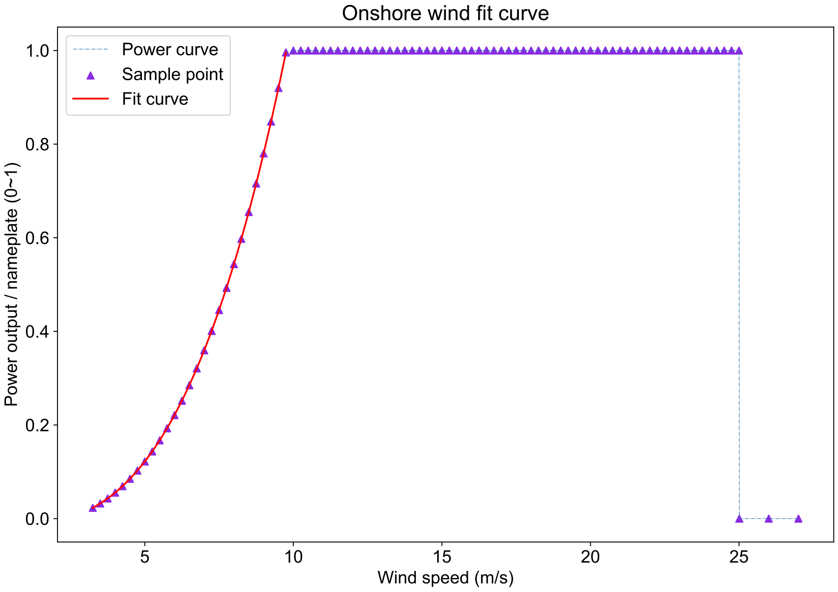

Figure S3: Illustration of the fitting results of the normalized power output curve for the selected wind turbine models.

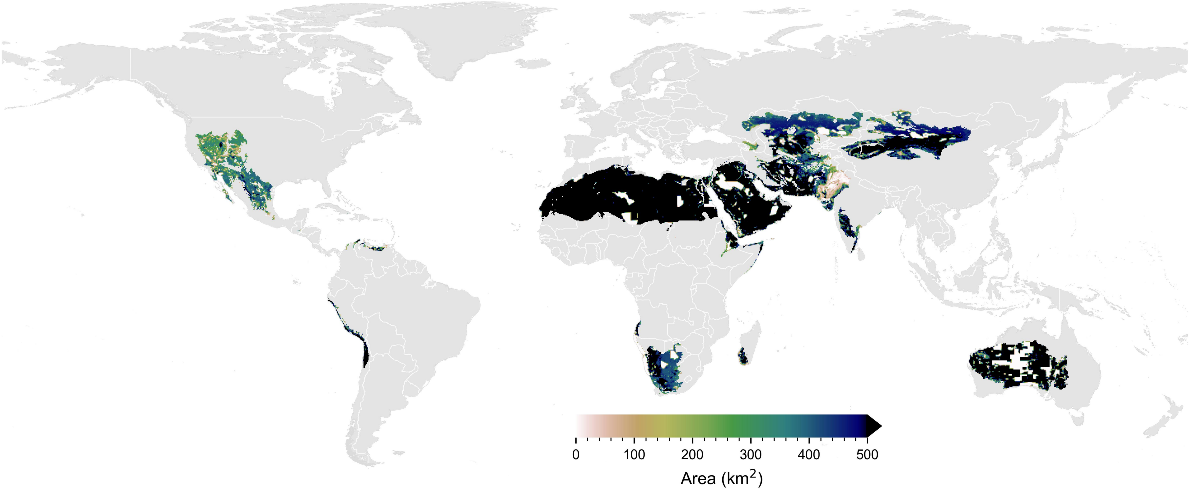

Figure S4: Suitable area assessed in this study for onshore wind power in the desert area.

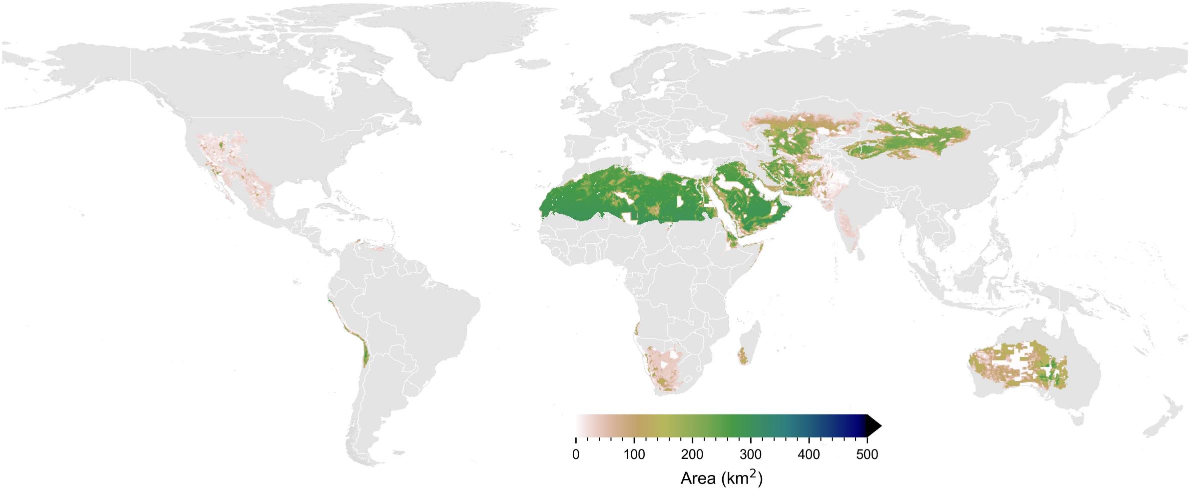

Figure S5: Suitable area assessed in this study for solar PV power in the desert area.

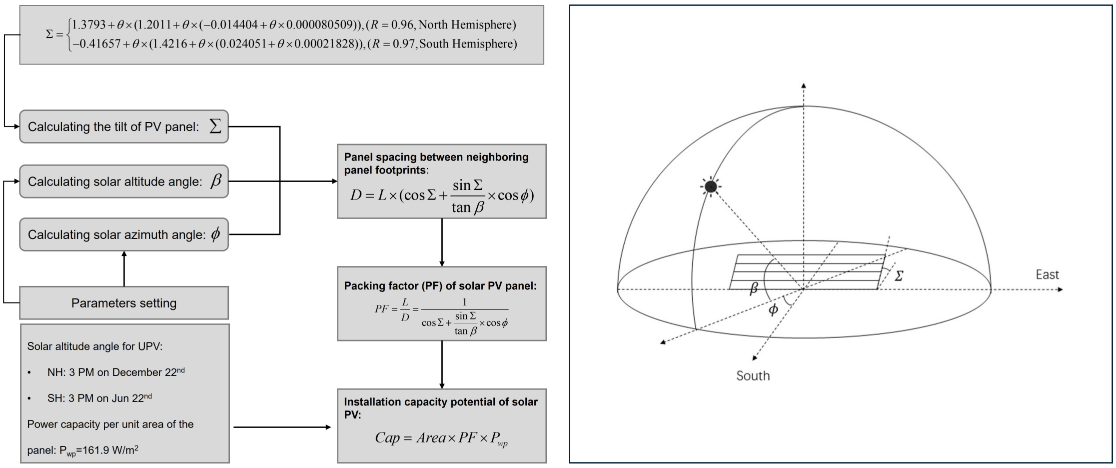

(a) Assessment schematic (b) PV tilt. Graphic: © Chen et al. 2019 [8]

Figure S6: Schematic diagram of installation capacity potential assessment for solar PV power.

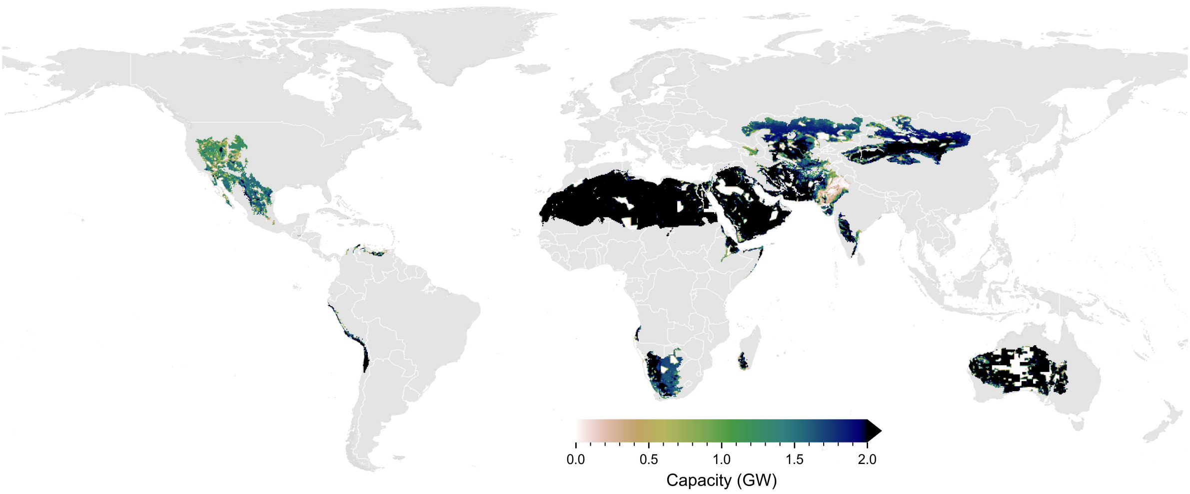

Figure S7: Installation capacity potential assessed in this study for onshore wind power in the desert area.

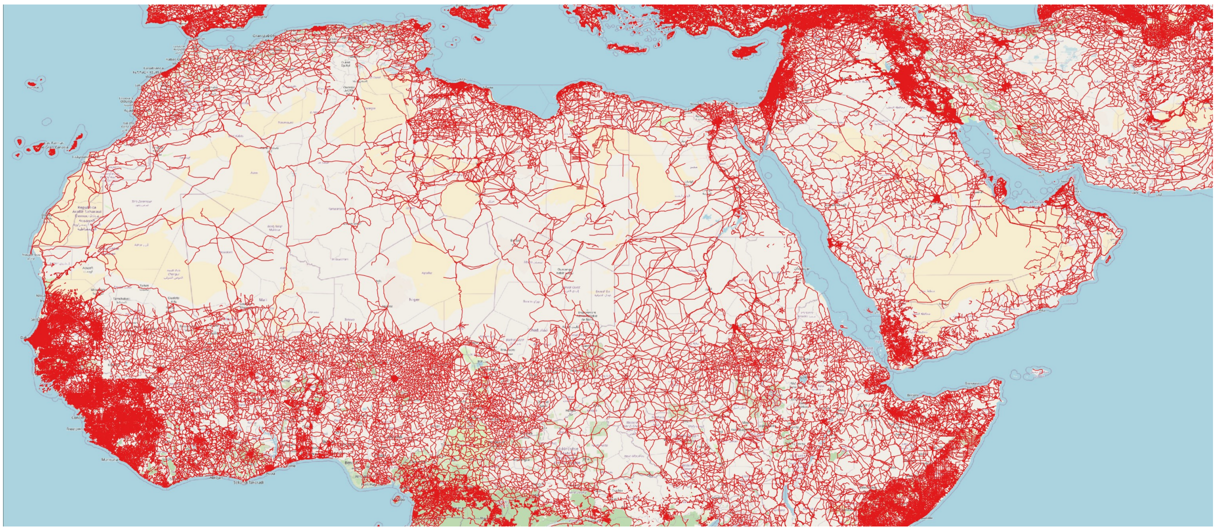

Figure S8: Illustration of existing roads around North Africa from the GRIP dataset.

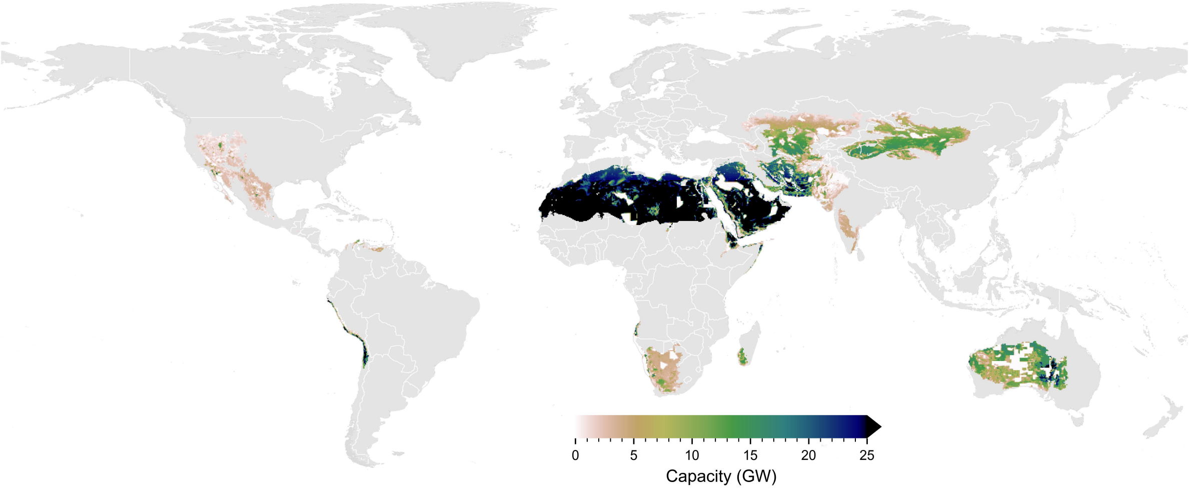

Figure S9: Installation capacity potential assessed in this study for solar PV power in the desert area.

4 Supplementary results

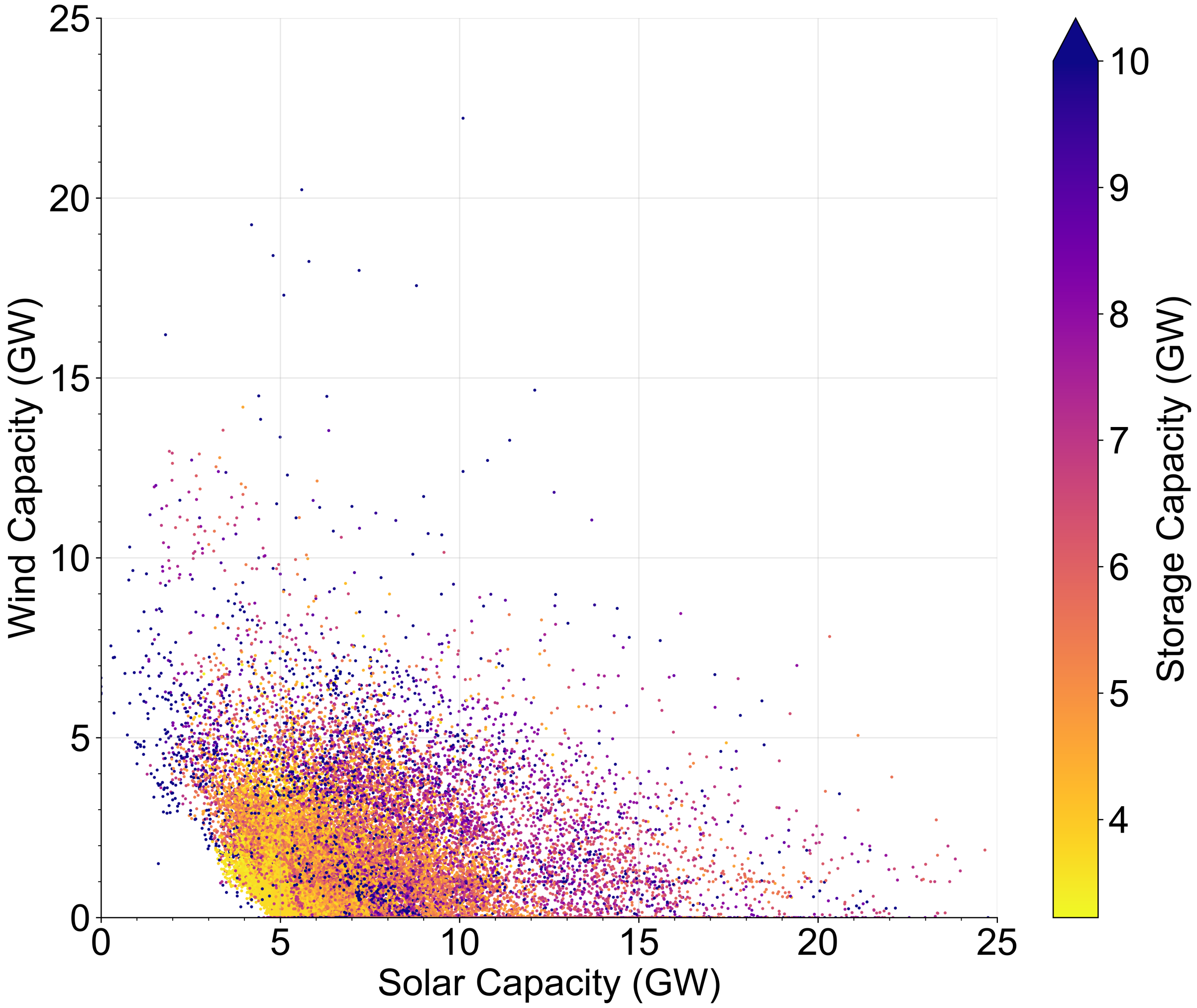

Figure S10: Distribution of WSS capacity combination across all grid cells.

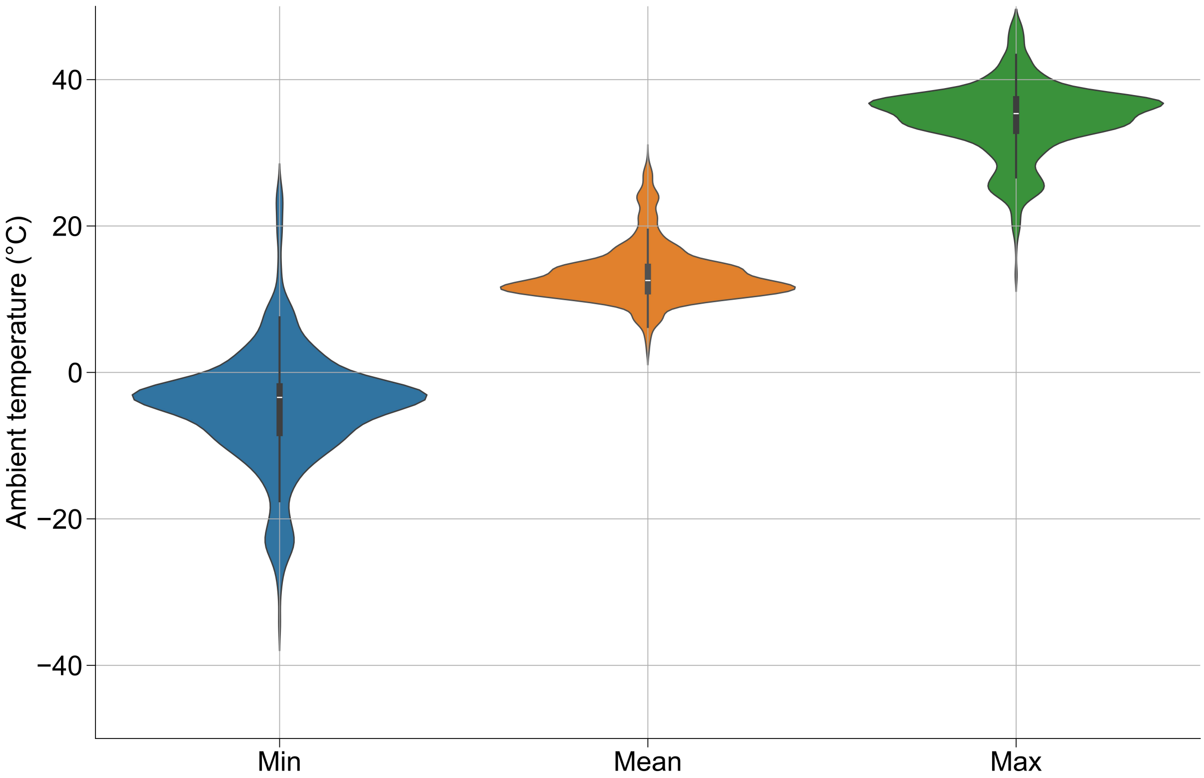

Figure S11: Violin plot of ambient temperature distribution of existing data centers.

References

[1] National Renewable Energy Laboratory. 2020 annual technology baseline: Nrel reference 7mw. `https://nrel.github.io/turbine-models/2020ATB_NREL_Reference_7MW_200.html`, 2020.

[2] Hans Hersbach, Bill Bell, Paul Berrisford, Shoji Hirahara, András Horányi, Joaquín Muñoz-Sabater, Julien Nicolas, Carole Peubey, Raluca Radu, Dinand Schepers, Adrian Simmons, Cornel Soci, Saleh Abdalla, Xavier Abellan, Gianpaolo Balsamo, Peter Bechtold, Gionata Biavati, Jean Bidlot, Massimo Bonavita, Giovanna Chiara, Per Dahlgren, Dick Dee, Michail Diamantakis, Rossana Dragani, Johannes Flemming, Richard Forbes, Manuel Fuentes, Alan Geer, Leo Haimberger, Sean Healy, Robin J. Hogan, Elías Hólm, Marta Janisková, Sarah Keeley, Patrick Laloyaux, Philippe Lopez, Cristina Lupu, Gabor Radnoti, Patricia Rosnay, Iryna Rozum, Freja Vamborg, Sebastien Villaume, and Jean-Noël Thépaut. The ERA5 global reanalysis. *Quarterly Journal of the Royal Meteorological Society*, 146(730):1999–2049, 2020.

[3] Yadong Lei, Zhili Wang, Deying Wang, Xiaoye Zhang, Huizheng Che, Xu Yue, Chenguang Tian, Junting Zhong, Lifeng Guo, Lei Li, et al. Co-benefits of carbon neutrality in enhancing and stabilizing solar and wind energy. *Nature Climate Change*, pages 1–8, 2023.

[4] Patrick R. Brown and Audun Botterud. The Value of Inter-Regional Coordination and Transmission in Decarbonizing the US Electricity System. *Joule*, 5(1):115–134, January 2021.

[5] Oleg A. Alduchov and Robert E. Eskridge. Improved Magnus Form Approximation of Saturation Vapor Pressure. *Journal of Applied Meteorology and Climatology*, 35(4):601–609, April 1996.

[6] Tianguang Lu, Peter Sherman, Xinyu Chen, Shi Chen, Xi Lu, and Michael McElroy. India's potential for integrating solar and on- and offshore wind power into its energy system. *Nature Communications*, 11(1):4750, 2020.

[7] Qiang Wang, Kun Luo, Renyu Yuan, Sanxia Zhang, and Jianren Fan. Wake and performance interference between adjacent wind farms: Case study of xinjiang in china by means of mesoscale simulations. *Energy*, 166:1168–1180, 2019.

[8] Shi Chen, Xi Lu, Yufei Miao, Yu Deng, Chris P. Nielsen, Noah Elbot, Yuanchen Wang, Kathryn G. Logan, Michael B. McElroy, and Jiming Hao. The Potential of Photovoltaics to Power the Belt and Road Initiative. *Joule*, 3(8):1895–1912, August 2019.

[9] Da Zhang, Ziheng Zhu, Shi Chen, Chongyu Zhang, Xi Lu, Xiliang Zhang, Xiaoye Zhang, and Michael R Davidson. Spatially resolved land and grid model of carbon neutrality in china. *Proceedings of the National Academy of Sciences*, 121(10):e2306517121, 2024.

[10] Patrick R Brown and Francis M O'Sullivan. Spatial and temporal variation in the value of solar power across united states electricity markets. *Renewable and Sustainable Energy Reviews*, 121:109594, 2020.

[11] A. P. Dobos. PVWatts Version 5 Manual. Technical Report NREL/TP-6A20-62641, National Renewable Energy Lab. (NREL), Golden, CO (United States), 2014.

[12] Sonia Jerez, Isabelle Tobin, Robert Vautard, Juan Pedro Montávez, Jose María López-Romero, Françoise Thais, Blanka Bartok, Ole Bøssing Christensen, Augustin Colette, Michel Déqué, Grigory Nikulin, Sven Kotlarski, Erik van Meijgaard, Claas Teichmann, and Martin Wild. The impact of climate change on photovoltaic power generation in Europe. *Nature Communications*, 6(1):10014, December 2015. Number: 1 Publisher: Nature Publishing Group.

[13] Shi Chen, Xi Lu, Yufei Miao, Yu Deng, Chris P. Nielsen, Noah Elbot, Yuanchen Wang, Kathryn G. Logan, Michael B. McElroy, and Jiming Hao. The potential of photovoltaics to power the belt and road initiative. *Joule*, 3:1895–1912, 8 2019.

[14] Xi Lu, Michael B McElroy, Chris P Nielsen, Xinyu Chen, and Junling Huang. Optimal integration of offshore wind power for a steadier, environmentally friendlier, supply of electricity in china. *Energy Policy*, 62:131–138, 2013.

[15] Muñoz Sabater, J. ERA5-Land hourly data from 1950 to present, Copernicus Climate Change Service (C3S) Climate Data Store (CDS). `https://cds.climate.copernicus.eu/cdsapp#!/dataset/reanalysis-era5-land?tab=overview`, 2019. DOI: 10.24381/cds.e2161bac (Accessed: 2024-02-25).

[16] Diego Silva Herran, Hancheng Dai, Shinichiro Fujimori, and Toshihiko Masui. Global assessment of onshore wind power resources considering the distance to urban areas. *Energy Policy*, 91:75–86, 2016.

[17] David EHJ Gernaat, Harmen Sytze de Boer, Vassilis Daioglou, Seleshi G Yalew, Christoph Müller, and Detlef P van Vuuren. Climate change impacts on renewable energy supply. *Nature Climate Change*, 11(2):119–125, 2021.

[18] Xinyu Chen, Yaxing Liu, Qin Wang, Jiajun Lv, Jinyu Wen, Xia Chen, Chongqing Kang, Shijie Cheng, and Michael B. McElroy. Pathway toward carbon-neutral electrical systems in China by mid-century with negative CO2 abatement costs informed by high-resolution modeling. *Joule*, 5(10):2715–2741, 2021.

[19] Xinyang Guo, Xinyu Chen, Xia Chen, Peter Sherman, Jinyu Wen, and Michael McElroy. Grid integration feasibility and investment planning of offshore wind power under carbon-neutral transition in China. *Nature Communications*, 14(1):2447, 2023.